ASSESSMENT OF THREE TURBULENCE MODEL PERFORMANCES IN PREDICTING WATER JET FLOW PLUNGING INTO A LIQUID POOL

by

Faiza ZIDOUNI KENDIL [1], ***Anis BOUSBIA SALAH*** [2*], ***and Amina MATAOUI*** [3]

[1]Nuclear Research Center of Brine, COMENA, Ain Oussera, Djelfa, Algeria
[2]Department of Mechanical and Nuclear Engineering, University of Pisa, Pisa, Italy
[3]Theoretical and Applied Fluid Mechanics Laboratory, Faculty of Physics, USTHB
Algiers, Algeria

Scientific paper
UDC: 532.529:517.95
DOI: 10.2298/NTRP1001013Z

The main purpose of the current study is to numerically investigate, through computational fluid dynamics modeling, a water jet injected vertically downward through a straight circular pipe into a water bath. The study also aims to obtain a better understanding of jet behavior, air entrainment and the dispersion of bubbles in the developing flow region. For these purposes, three dimensional air and water flows were modeled using the volume of fluid technique. The equations in question were formulated using the density and viscosity of a "gas-liquid mixture", described in terms of the phase volume fraction.
Three turbulence models with a high Reynolds number have been considered *i. e.* the standard k-ε model, realizable k-ε model, and Reynolds stress model. The predicted flow patterns for the realizable k-ε model match well with experimental measurements found in available literature. Nevertheless, some discrepancies regarding velocity relaxation and turbulent momentum distribution in the pool are still observed for both the standard k-ε and the Reynolds stress model.

Key words: water jet, turbulence modeling, VOF model, realizable k-ε model, Reynolds stress model, standard k-ε model

INTRODUCTION

Advanced computational methods, such as computational fluid dynamics (CFD), have now been recognized as important tools that allow detailed modeling, under single and two-phase flows, of the velocity, pressure and temperature fields with a high degree of accuracy. An important and challenging aspect concerns liquid injected into a gaseous medium. Such phenomenon is a crucial matter in many industrial topics ranging from ink-jet printing, direct fuel injection in diesel engines, minerals-processing floatation cells, to emergency core cooling of a pressurized water nuclear reactor.

CFD modeling is considered hereafter, since it allows useful insight into highly complex flows in the jetting system. Indeed, when a plunging jet impinges into a liquid pool, air bubble entrainment will occur in the form of a local, singular aeration [1, 2]. The mechanisms of bubble entrainment depends upon jet velocity at the impact, physical properties of the fluid, jet nozzle design, length of the free-falling jet and jet turbulence [1]. For small jet velocities larger than the threshold velocity, so called onset velocity, air is entrained in the form of individual air bubbles. At larger jet velocities, large packets of air are entrained and subsequently broken up in the shear flow.

Several researchers have shown interest in circular plunging jets [1, 3]. Numerous experiments were performed with small circular jets (*i. e.* less than 5 mm in diameter) for which mostly qualitative studies were performed. Only a limited number of researchers studied the flow field below the impingement. McKeogh and Ervine [4] and Van de Donk [5] recorded air concentration profiles and velocity distributions primarily in the fully developed flow region, while Bonetto *et al.* [6] presented results obtained in both developing and fully developed flow regions. Bin [1] and Chanson [2], highlighted the lack of information on air content dis-

* Corresponding author; e-mail: anis6622@googlemail.com

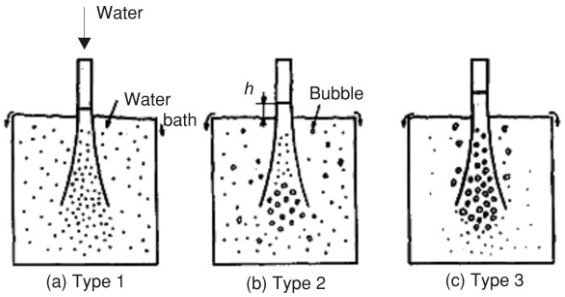

Figure 1. Three types of bubble dispersion patterns [8]

tributions in the vicinity of the impingement point and entrained bubble size distributions. However, physical modeling of plunging jet flows remains subject to scaling effects which have not been properly explained as of yet [2, 7].

Shakouchi *et al*. [8] have investigated vertical water jet plunging into a water pool and reported three types of bubble dispersion patterns in cases where the plunging water jet impacts the bath surface before its breakup, as shown schematically in fig. 1. When the distance from the pipe exit to the undisturbed bath surface is short, and accordingly, the surface of the water jet is smooth, a lot of small bubbles are generated and they disperse throughout the bath (type 1).

On the other hand, when the distance is long and the surface of the water rough, relatively large bubbles are generated and the bubble dispersion region is localized beneath the pipe exit (type 3). Bubble dispersion patterns of type 1 and 3 appear simultaneously for the intermediate distance (type 2). Exact knowledge of the boundaries among these three regimes has, however, not been obtained. As opposed to this, turbulence characteristics in bubbly flows induced by a plunging water jet into a water bath are well documented.

Iguchi *et al*. [9] recaptured experiments with the same flow field and deduced that bubble entrainment is mainly related to shear flow instabilities on the plunging jet surface. Additional turbulence production in the wake of bubbles also affects the development of the flow in the water bath. More information on these characteristics would be useful for the purpose of this study.

In fact, this work investigates appropriate turbulence models for simulating a vertical water jet plunging into a water pool. The assessment is performed using three turbulence models: the standard k-ε, realizable k-ε, and the Reynolds stress model. This is followed by comparative studies of the simulation results and experimental measurements by Iguchi *et al*. [9].

In the plunging jet configuration, gas has two different morphologies (see fig. 2). The gas above the water level is a continuous phase, whereas the gas below the water level is the dispersed phase. In order to model this flow, two approaches are possible. The one using the Euler-Euler method with two phases: one for

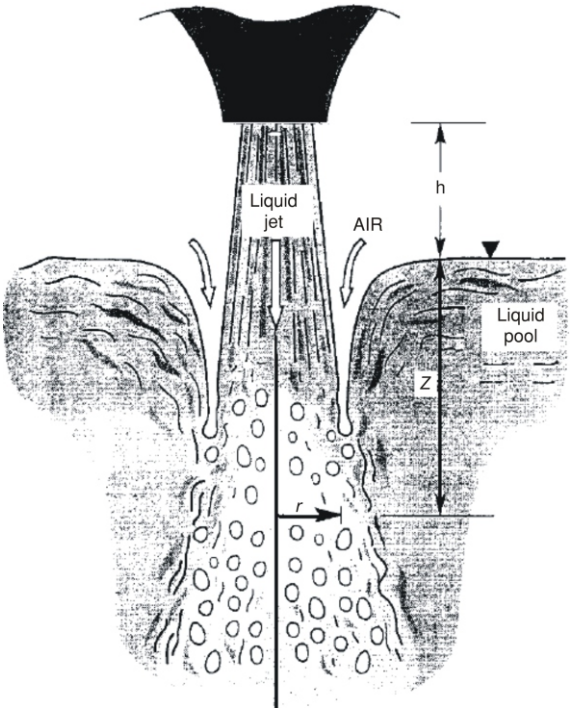

Figure 2. Morphologies of the phases near an impinging jet [10]

water (continuous phase) and the other for the gas (dispersed phase). The different morphologies of the gas then have to be reflected by different coefficients in closures for the momentum transfer between the gas and water phases. In the second approach, one can use only one homogeneous phase with a surface reconstruction. This model is recommended for stratified or non-interpenetrating flows. In this approach, the morphologies of the gas have to be reconstructed using the reconstitution of the interface algorithm which represents the free surface (air water) as a sharp discontinuity. Since gas and liquid flows do not interpenetrate in the considered cases, a calculation with the volume of fluid (VOF) approach has been chosen. The VOF model enables the computation of two-phase flows where the phases do not mix, so the gas-liquid interface is clearly identified.

MAIN CONSERVATION EQUATIONS

In this simulation, the governing equations in the three dimensional coordinate systems are solved using the commercial CFD code FLUENT.

The jetting system considered herein is governed by gas and liquid flows and, as stated in the aforementioned paragraph, can be modeled using the VOF technique (Hirt *et al*.) [11]. The latter is based upon the fixed grid technique designed for two or more immiscible fluids (or phases), where the position of the interface is of the utmost interest.

Mass equation

In the VOF model, the volume fraction of each of the phases in each computational cell is tracked throughout the computational domain. In addition to the velocity and pressure, volume fraction is also a variable of the flow field in the VOF technique and, hence, contained in both mass and momentum equations.

The continuity equation for the liquid (primary phase) with a volume fraction φ, has the following form

$$\frac{\partial \varphi}{\partial t} \quad u \operatorname{div} \varphi \quad 0 \tag{1}$$

where the secondary phase volume fraction is

$$\varphi_{\mathrm{g}} \quad 1 \quad \varphi \tag{2}$$

and the properties of these phases are defined as

$$\rho \quad \rho_{\mathrm{g}} (1 \quad \varphi) \quad \rho_{\mathrm{l}} \varphi \tag{3}$$

$$\mu \quad \mu_{\mathrm{g}} (1 \quad \varphi) \quad \mu_{\mathrm{l}} \varphi \tag{4}$$

Momentum equation

The momentum equation for the computational domain in its generalized form can be written as

$$\frac{\partial \rho u}{\partial t} \quad \operatorname{div} \rho u \quad \operatorname{grad}(p) + \operatorname{div} \mu[\operatorname{grad}(\mathrm{u})] + \rho \mathrm{g} \tag{5}$$

where g is the acceleration due to gravity, p – the fluid pressure, ρ and μ are the density and viscosity based on eqs. (3) and (4), respectively.

Turbulent flow equations

Since the liquid and gas velocity exiting the nozzles is relatively high, it is appropriate to simulate the flow in the jetting system using a turbulent flow model. To do this, the flow variables, such as that of ϕ, and fluctuation ϕ , correspond in a standard way, so that: $\phi = \phi + \phi$. Inserting the decomposed variables to the instantaneous equation and applying the Reynolds averaging, yield a set of Reynolds averaged conservation equations for mass and momentum, as well as for turbulence kinetic energy, k, and its dissipation rate ε. For convenience, and in order to drop overbear on the mean variables, the Reynolds averaged equation can be written in the following generic transport equation form

$$\frac{\partial}{\partial t}(\rho k) \quad \frac{\partial}{\partial x_i}(\rho k u_i)$$
$$\frac{\partial}{\partial x_j} \quad \mu \quad \frac{\mu_{\mathrm{t}}}{\sigma_k} \frac{\partial k}{\partial x_j} \quad G_{\mathrm{k}} \quad G_{\mathrm{b}} \quad \rho \varepsilon \quad Y_{\mathrm{M}} \quad S_k \tag{6}$$

$$\frac{\partial}{\partial t}(\rho \varepsilon) \quad \frac{\partial}{\partial x_i}(\rho \varepsilon) = \frac{\partial}{\partial x_i} \quad \mu \quad \frac{\mu_t}{\sigma_k} \frac{\partial \varepsilon}{\partial x_j}$$
$$C_{1\varepsilon} \frac{\varepsilon}{k}(G_k \quad C_{3\varepsilon} G_b) \quad C_{2\varepsilon} \rho \frac{\varepsilon^2}{k} \quad S_\varepsilon \tag{7}$$

where G_{k} is the generation of kinetic energy of the turbulence due to mean velocity gradients, G_{b} – the generation of kinetic energy of turbulence due to buoyancy, Y_{k} represents the contribution of the fluctuating dilatation in compressible turbulence to the overall dissipation rate, $C_{1\varepsilon}$, $C_{2\varepsilon}$, and $C_{3\varepsilon}$ are constants, σ_k and σ_ε are the turbulent Prandtl numbers for k and σ, respectively, and S_k and S_ε are the user-defined source terms.

CLOSURE EQUATIONS

The solutions of conservation equations are obtained through the following closure relations.

Standard energy dissipation model

Turbulent (or eddy) viscosity, μ_{t}, is computed by combining k and ε as follows

$$\mu_{\mathrm{t}} \quad \rho C_\mu \frac{k^2}{\varepsilon} \tag{8}$$

where C_μ is a constant, while model constants $C_{1\varepsilon}$, $C_{2\varepsilon}$, C_μ, σ_k, and σ_ε have the following default values: $C_{1\varepsilon}$ = = 1.44, $C_{2\varepsilon}$ =1.92, C_μ = 0.09, σ_k = 1.0, σ_ε = 1.3

These default values have been determined from experiments with air and water for fundamental turbulent shear flows, including homogeneous shear flows and decaying isotropic grid turbulence. They have been found to work fairly well for a wide range of wall-bounded and free shear flows.

Realizable *k-ε* turbulence model

The realizable *k-ε* model is a relatively recent development, differing from the standard *k-ε* model in two crucial ways:

- the realizable *k-ε* model contains a new formulation of turbulent viscosity, and
- a new transport equation for the dissipation rate ε has been derived from an exact equation for the transport of the mean-square vortices fluctuation.

The word "realizable" means that the model is able to mathematically determine certain Reynolds stress tensor components, in agreement with the physics of turbulent flows. An immediate benefit of the realizable *k-ε* model is that it predicts more accurately the spreading rate of both planar and round jets. It is also likely to provide superior performance for flows involving rotation, boundary layers under strong adverse pressure gradients, separation, and recirculation, all of which is important in our case.

The *s* realizable *k-ε* model considers the combination of the Boussinesq relationship and the eddy viscosity definition to obtain the following expression for the normal Reynolds stress in an incompressible strained mean flow

$$\overline{u^2} \quad \frac{2}{3}k \quad 2\upsilon_t \frac{\partial U}{\partial x} \tag{9}$$

using eq. (8), for calculating $\upsilon_t = \mu_t/\rho$, it can be obtained that the normal stress, $\overline{u^2}$ which by definition is a positive quantity, becomes negative, *i. e.*, "non-realizable", when the strain is large enough to satisfy

$$\frac{k}{\varepsilon}\frac{\partial U}{\partial x} \quad \frac{1}{3C_\mu} \quad 3.7 \tag{10}$$

Similarly, it can also be shown that the Schwarz inequality for shear stresses ($\overline{u_\alpha u_\beta}^2 \quad \overline{u_\alpha^2 u_\beta^2}$) no summation over α and β) can be violated when the mean strain rate is large.

The most straightforward way to ensure the realizability (positivity of normal stresses and Schwarz inequality for shear stresses) is to make C_μ variable by sensitizing it to the mean flow (mean deformation) and the turbulence *k–ε* as describe below

$$C_\mu \quad \frac{1}{A_0 \quad A_s\frac{kU^*}{\varepsilon}}$$

where

$$\widetilde{\Omega}_{ij} \quad \Omega_{ij} \quad 2\varepsilon_{ijk}\omega_k \quad U^* \quad \sqrt{S_{ij}S_{ij} \quad \widetilde{\Omega}_{ij}\widetilde{\Omega}_{ij}}$$
$$\Omega_{ij} \quad \overline{\Omega_{ij}} \quad \varepsilon_{ijk}\omega_k$$

where $\overline{\Omega_{ij}}$ is the mean rate-of-rotation tensor viewed in a rotating reference frame with the angular velocity ω_k. Model constants A_0 and A_s are given by

$$A_0 = 4.04 \quad \text{and} \quad A_s \quad \sqrt{6}\cos\phi$$
$$\phi \quad \frac{1}{3}\cos^{-1}\sqrt{6}W, \; W \quad \frac{S_{ij}S_{jk}S_{ki}}{\widetilde{S}^3}, \; \widetilde{S} \quad \sqrt{S_{ij}S_{ij},}$$

where

$$S_{ij} \quad \frac{1}{2}\left(\frac{\partial u_j}{\partial x_i} \quad \frac{\partial u_i}{\partial x_j}\right)$$

In CFD FLUENT computation, the term $-2\varepsilon_{ijk}\omega_k$ is, by default, not included in the calculation of $\widetilde{\Omega}_{ij}$. This is an extra rotation term that is not compatible with cases involving sliding meshes or multiple reference frames.

Transport equations for the realizable *k-ε* model

The modeled transport equations for *k* and *ε* in the realizable *k-ε* model are

$$\frac{\partial}{\partial t}(\rho k) \quad \frac{\partial}{\partial x_j}(\rho k u_j)$$
$$\frac{\partial}{\partial x_i}\left(\mu + \frac{\mu_t}{\sigma_k}\frac{\partial k}{\partial x_j}\right) \quad G_k \quad G_b \quad \rho\varepsilon \quad Y_M \quad S_k \tag{11}$$

$$\frac{\partial}{\partial t}(\rho\varepsilon) \quad \frac{\partial}{\partial x_j}(\rho\varepsilon u_j) \quad \frac{\partial}{\partial x_j}\left(\mu \quad \frac{\mu_t}{\sigma_\varepsilon}\frac{\partial \varepsilon}{\partial x_j}\right)$$
$$+\rho C_1 S_\varepsilon \quad \rho C_2 \frac{\varepsilon^2}{k \quad \sqrt{\upsilon\varepsilon}} \quad C_{1\varepsilon}\frac{\varepsilon}{k}C_{3\varepsilon}G_b \quad S_\varepsilon \tag{12}$$

where $C_1 \quad \max[0.43, \eta/(\eta \quad 5)]$, $\eta \quad S(k/\varepsilon)$, and the mean rate-of-strain tensor $S \quad (2S_{ij}S_{ij})^{1/2}$.

Model constants C_2, σ_k, and σ_ε have been established to ensure that the model performs well for certain canonical flows. The model constants are $C_{1\varepsilon}$ = = 1.44, $C_2 = 1.9$, $\sigma_k = 1.0$, $\sigma_\varepsilon = 1.2$.

Reynolds stress turbulence model

In general, when the turbulence kinetic energy is needed for modeling a specific term, it is obtained by taking the trace of the Reynolds stress tensor

$$k \quad \frac{1}{2}\overline{u_i u_i} \tag{13}$$

The exact transport equations for the transport of Reynolds stresses, $\rho\overline{u_i u_j}$, may be written as follows

$$\underbrace{\frac{\partial}{\partial t}(\overline{u_i u_j})}_{\text{local time derivation}} \quad \underbrace{\frac{\partial}{\partial x_k}(\rho u_k \overline{u_i u_j})}_{C_{ij} \quad \text{convection}}$$
$$\underbrace{\frac{\partial}{\partial x_k}\left[\overline{\rho u_i u_j u_k} \quad \overline{p(\delta_{kj}u_i \quad \delta_{ik}u_j)}\right]}_{D_{T,ij} \quad \text{turbulent diffusion}}$$
$$\underbrace{\frac{\partial}{\partial x_k}\left(\mu\frac{\partial}{\partial x_k}(\overline{u_i u_j})\right)}_{D_{L,ij} \quad \text{molecular diffusion}} \quad \underbrace{\rho\left(\overline{u_j u_k}\frac{\partial u_j}{\partial x_k} \quad \overline{u_j u_k}\frac{\partial u_j}{\partial x_k}\right)}_{P_{ij} \quad \text{stress production}}$$
$$\underbrace{\rho\beta(g_i\overline{u_j\theta} \quad g_j\overline{u_i\theta})}_{G_{ij} \quad \text{buoyancy production}} \quad \underbrace{\overline{p\left(\frac{\partial u_i}{\partial x_j} \quad \frac{\partial u_j}{\partial x_i}\right)}}_{f_{ij} \quad \text{pressure strain}} \quad \underbrace{2\mu\overline{\frac{\partial u_i}{\partial x_k}\frac{\partial u_j}{\partial x_k}}}_{e_{ij} \quad \text{dissipation}}$$
$$\underbrace{2\rho\Omega_k(\overline{u_j u_m}\varepsilon_{ikm} \quad \overline{u_i u_m}\varepsilon_{jkm})}_{F_{ij} \quad \text{production by system rotation}} \quad \underbrace{S_{\text{user}}}_{\text{source term}} \tag{14}$$

Convection term C_{ij}, molecular diffusion $D_{L,ij}$, stress production, P_{ij}, and production by system rotation term F_{ij}, do not require modeling, but other terms need modeling in order to close a system of differential equations. The dissipation tensor, ε_{ij}, is modeled as

$$\varepsilon_{ij} \quad \frac{2}{3}\delta_{ij}(\rho\varepsilon \quad Y_M) \tag{15}$$

where $Y_M \quad 2\rho\varepsilon M_t^2$ is an additional "dilatation dissipation".

The turbulent Mach number in this term is defined as: $M_t \quad (k/a^2)^{1/2}$
where $a \quad (\gamma RT)^{1/2}$ is the sound velocity. This compressibility modification always takes effect when the compressible form of the ideal gas law is used.

The scalar dissipation rate ε is computed with a model transport equation similar to that used in the standard k-ε model

$$\frac{\partial}{\partial t}(\rho\varepsilon) \quad \frac{\partial}{\partial x_i}(\rho\varepsilon u_i) \quad \frac{\partial}{\partial x_j} \quad \mu \quad \frac{\mu_t}{\sigma_\varepsilon} \quad \frac{\partial \varepsilon}{\partial x_j}$$
$$C_{\varepsilon 1} \frac{1}{2}[P_{ii} \quad C_{\varepsilon 3} G_{ii}] \frac{\varepsilon}{k} \quad \rho C_{\varepsilon 2} \frac{\varepsilon^2}{k} \quad S_\varepsilon \qquad (16)$$

where $\sigma_\varepsilon = 1.0$, $C_{1\varepsilon} = 1.44$, $C_{\varepsilon 2} = 1.92$, $C_{\varepsilon 3}$ is evaluated as a function of the local flow direction relative to the gravitational vector, and S_ε is a user-defined source term, not considered in this study.

Turbulent viscosity, μ_t, is computed in the same manner as in k-ε models, according to eq. (8) with $C_\mu = 0.09$.

COMPUTATIONAL MODELING PARAMETERS

Modeling parameters

Figure 3 provides a schema of the experimental apparatus referring to Iguchi *et al*. [9] and McKeogh *et al*. [4]. The vessel has an inner diameter (D) of 20.0 cm, while the vessel diameter is 20 cm with a height (H) of 39.0 cm. The origin of the cylindrical coordinate system is placed on the undisturbed bath surface. Axial and radial coordinates are denoted by z and r, respectively. The corresponding velocity components were designated by u and v. The water is injected through a straight circular pipe (having an inner diameter d of 0.5 cm and a length L of 60 cm) into a water bath. The plunging water jet impinges perpendicularly to the water surface.

The inlet conditions were also determined by consulting the previous investigators [4, 9]. The plunging water jet flow rate Q_w is 50 cm^3/s. The corresponding mean pipe exit velocity at $\bar{u}_0$ (= 4 Qw/ d^2) is 254 cm/s.

The pipe Reynolds number is higher than 10^4 and the respective ratio L/d is 120. Accordingly, the water flow in the pipe is turbulent and fully developed at the pipe exit. At the location, turbulence intensity increased monotonically from approximately 5% in the central part, to approximately 15% in the outer part of the pipe. These turbulence intensities are described here because they affect the behavior of the bubbles significantly [1].

Geometry and grid arrangement

The geometry and computational domain used to model the jetting system are shown in fig. 4. The symmetry of the configuration allowed us to consider a quarter domain for the computation. A three-dimensional computational domain is considered using a non-uniform meshing grid by the tetrahedral scheme; with this scheme, clustering is automatically made towards the centerline of the water jet direction. Grid contraction toward the free surface is required for capturing the gas and liquid flows and the deformation of the gas-liquid interface.

The uncertainty in numerical results is assessed by checking the convergence through mesh refinement calculations for simulations of two plunging wa-

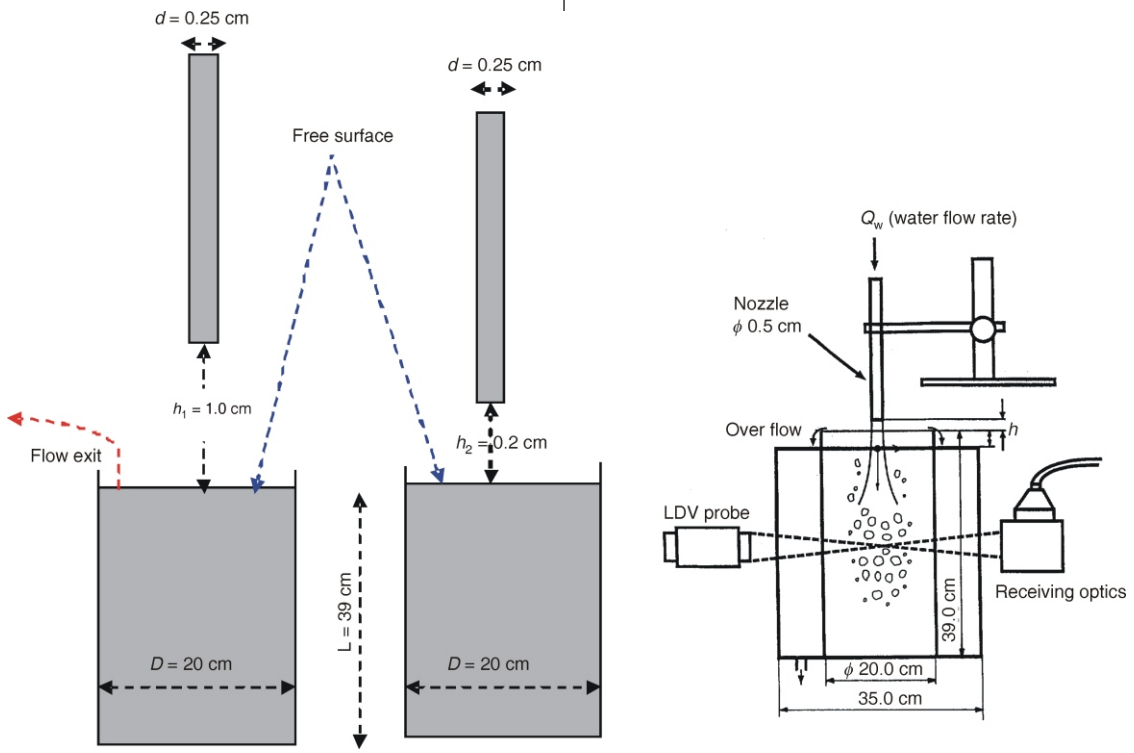

Figure 3. Schematic of experimental apparatus, Iguchi *et al.* [9]

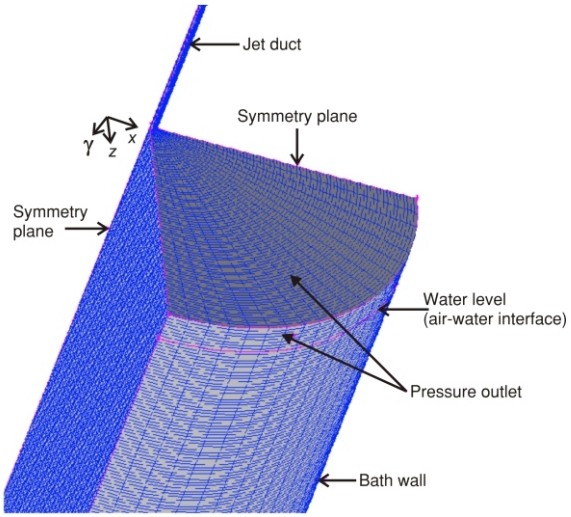

Figure 4. Computational grid arrangement

ter jet configurations. For this purpose, the following cases were computed for: (a) $\delta x_i = 0.4$ mm; (b) $\delta x_i = = 0.223$ mm; (c) $\delta x_i = 0.2$ mm. The results are afterwards compared for contours φ at various simulation times in the center line velocity profile. Calculations show that the mesh sizes used in case (b) were adequate for this kind of jet simulations, since no difference was noted when compared with case (c). Further mesh refinement and numerical tests were carried out to check the stability of the plunging jet flow simulation.

The position of the surface of the liquid is estimated by plotting contours of equal value to the air volume fraction φ. The value of $\varphi = 10^{-4}$ is used to determine the position of the jet interface. Time step δt, is set by considering the maximum attainable velocity v of the fluid in one direction (x_i). It is limited by the Courant number, $\delta t/(\delta x/u) < 0.25$. For most simulations reported here, δt is fixed at 1 10^{-5} s.

The used spatial discretisation was performed by the QUICK interpolation scheme, while the higher-order differences scheme is used for time stepping. The under-relaxation parameters for pressure and velocity are usually set to a value of 0.2.

Boundary conditions

Four types of boundary conditions were used to predict the flow field within the computational domain.

Water jet inlet

The condition of the nozzle is important in predicting center line velocity and shear stress. In this work, a uniform velocity profile is considered. The imposed inlet velocity boundary conditions at the nozzle are expressed by

$$U = U_{\text{inlet}},$$
$$V = 0 \text{ and } W = 0$$
$$k = k_{\text{inlet}} = 1.5(U_{\text{inlet}} I)^2$$
$$\varepsilon = \varepsilon_{\text{inlet}} = (C_\mu)^{3/4} \frac{(k_{\text{inlet}})^{3/2}}{l}$$

where the turbulence length scale at the inlet is assumed to be the nozzle opening. Turbulence intensity, I, is assumed to be 10% of the mean inlet velocity magnitude.

Solid boundaries

Wall boundary conditions are used at the solid boundary of the liquid pool where no slip boundary conditions were imposed. For the evaluation of the wall effect on turbulence, the logarithmic near wall function approach [12] has been used to model the wall bounded turbulent flows. The semi empirical formula is used to bridge the velocity affected region (viscous sub layer and buffer layer) between the wall and the fully turbulent region.

Exit boundaries

The exit water boundary considers a non-fully developed flow. In fact, it is found that reversed flows can occur at this boundary, indicating that the fluid motion is not fully developed. Consequently, the pressure outlet boundary is assumed.

Symmetry

Symmetry boundaries are used to reduce the computational domain to a symmetric subsection of the overall physical system. The normal gradients of all flow variables are thus zero at the symmetry plane. The symmetry boundary condition can therefore be summarized as:

– zero normal velocity at a symmetry plane, and
– zero normal gradients of all variables at a symmetry plane.

RESULTS AND DISCUSSION

In general, after about 10 s of the simulated physical time, the transient VOF-RANS calculations become steady. For a good accuracy of the simulated flow, the times step is relatively small ($\Delta t = 10^{-5}$).

Bubble behavior

Figure 5 describes bubble behavior in the vessel for the two distances of the exit water jet. The Iguchi experiments estimated the penetration depth H_p of the large bubbles with a diameter of around 0.4 cm to be larger than 30 cm for $h = 0.2$ cm and 23 cm for $h = 1$ cm.

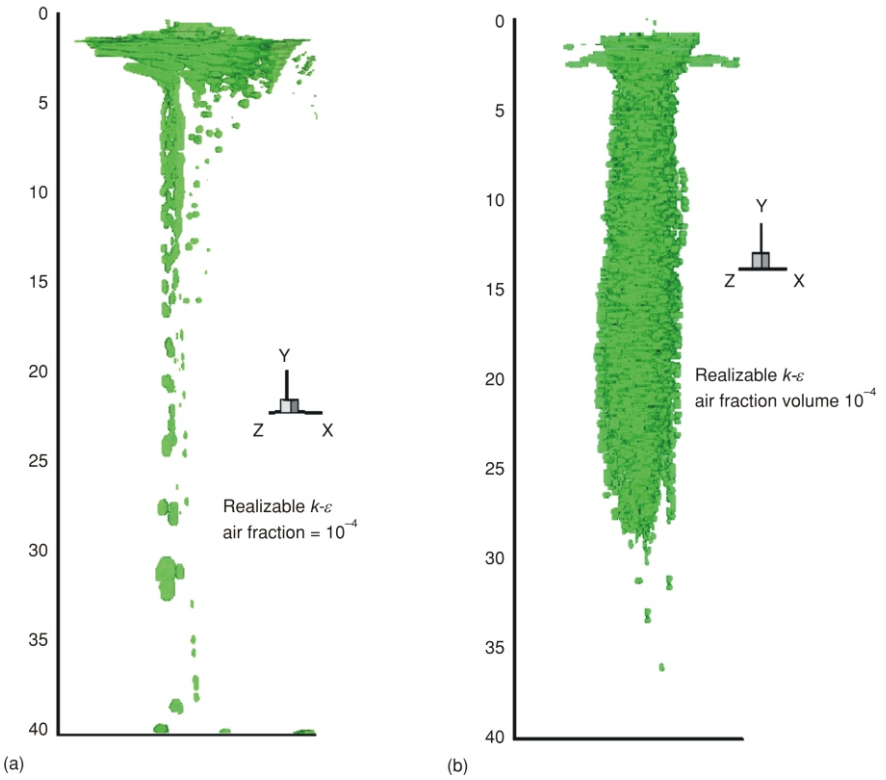

Figure 5. Air bubbles behavior when jet impinges the vessel
(a) water jet configuration h = 1 cm; (b): water jet configuration h = 0.2 cm

The agreement between the experiment and the simulation is quite good for configuration (b). For configuration (a), the bubbles attain the bottom of the wall. This discrepancy from the experimental observation can be explained as follows: when cells, mainly large cells, contain more than one bubble, the reconstitutive interf

ace method cannot reconstitute them individually, collapsing them instead in one larger bubble. The possible solution is to adopt smaller cells in this region, but in this case, the computational time becomes extremely large.

Distribution of the axial mean velocity of the bubble dispersion region

Looking at the axial velocity profile in fig. 6(a) and 6(b) corresponding to configurations where $h = 1$ cm and $h = 0.2$ cm, respectively, it can be said that no standard k-ε model or Reynolds stress model matches accurately the experimental data.

The realizable k-ε turbulence model predicts the velocity profile for the two configurations much better. Some discrepancies appear at a deeper distance ($z > 15$cm) for the configuration where $h = 1$cm. This is explained as follows: the maximum bubble diameter for $h = 1$ cm is much larger than that of $h = 0.2$ cm,

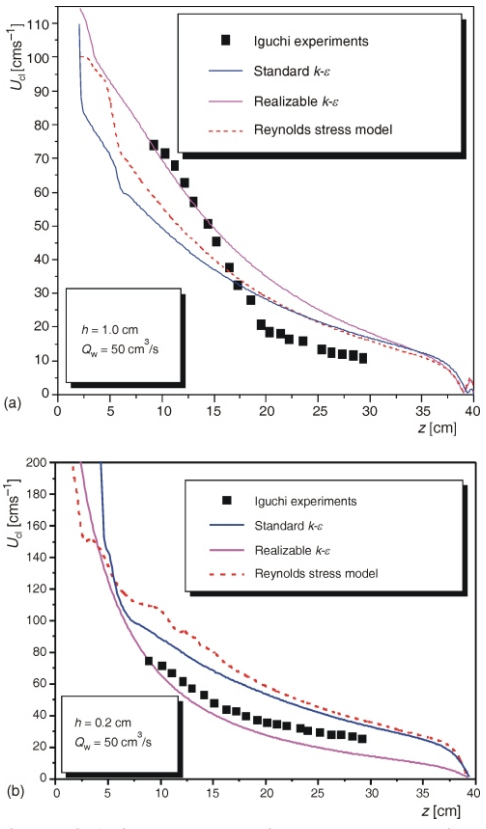

Figure 6. Axial mean velocity on the center line
(a) water jet configuration h = 1 cm;
(b) water jet configuration h = 0.2 cm

thus the buoyancy forces play a more important role for $h = 1$ cm than for $h = 0.2$ cm. As a result, the downward water motion for $h = 1$ cm (flow type 3 in fig. 3) is highly suppressed for $z > 15$ cm. To eliminate such discrepancies, an elaborated two-phase flow model can be proposed with a realizable k-ε model.

Turbulence components on the centerline of the bubble dispersion region

In figs. 7(a) and 7(b), the standard k-ε model slightly under-predicts the turbulence kinetic energy, while the Reynolds stress model's prediction is much higher. The realizable k-ε model is found to perform and model this flow characteristic much better than the standard k-ε.

Regarding the Reynolds stress model, the results are fairly unexpected, because this model is designed so as to predict more complex flows, such as anisotropic flows with strong curvatures. This can be attributed to the limitation of the homogenous-VOF model. In fact, this model uses a lot of assumptions, such as the one of a single velocity for air and water, neglecting the buoyancy effect and the additional turbulence added by the migration of bubbles. Nevertheless, further investigations using more elaborate and sophisticated models are needed.

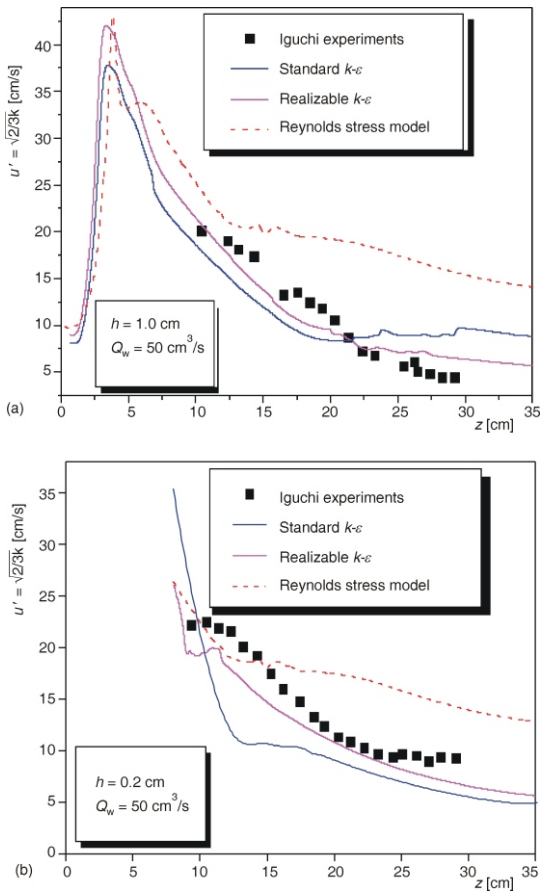

Figure 7. Velocity fluctuation on the center line
(a) water jet configuration h = 1 cm;
(b) water jet configuration h = 0.2 cm

Turbulent kinetic energy contours

As stated in the experimental observations of Iguchi *et al*. [9], the flow configuration for $h = 1$ cm ($Q_w = 50$ cm^3/s) corresponds to flow type 3 and that of $h = 0.2$ cm ($Q_w = 50$ cm^3/s) corresponds to flow type 1 in fig. 3.

According to these experimental observations, we can assume that the kinetic energy contours for these two configurations ($h = 1$ cm and $h = 0.2$ cm) are as expected. The local maxima of kinetic energy corresponds, more or less, to the two lateral eddies on each side of the jet.

For flow pattern type 3, relatively large bubbles are generated and the bubble dispersion region is localized beneath the pipe exit; for this reason, the shear layer is close to the jet axis as observed in fig. 8(a), corresponding to the maximum kinetic energy.

But, for the flow pattern type 1, a number of small bubbles are generated and they disperse in the bath, so the shear layer is slightly off the jet axis which makes the maximum kinetic energy maximum located around the jet axis (see fig. 8b), corresponding to the configuration $h = 0.2$ cm.

CONCLUDING REMARKS

Nowadays, multi-dimensional modeling of flows is being intensively investigated in order to obtain more accurate simulations of complex phenom-

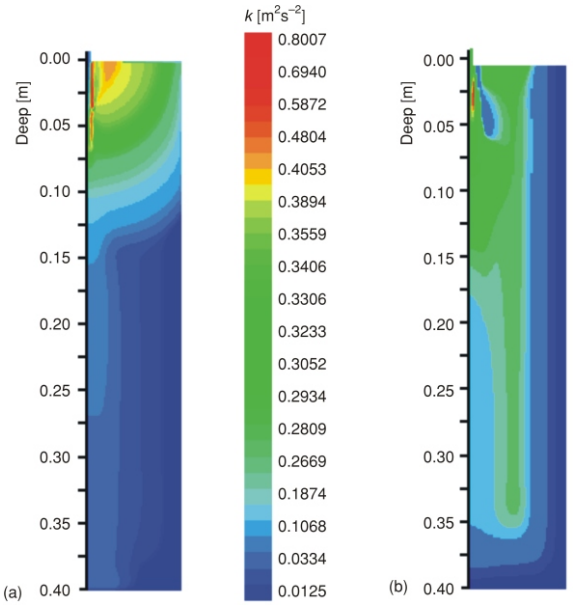

Figure 8. Turbulence energy contours in the water bath for the two flow configurations
(a) water jet configuration h = 1 cm;
(b) water jet configuration h = 0.2 cm

ena encountered in the industry [13]. In this paper, a particular phenomenon related to a vertical injection of water downward onto a water bath through a circular pipe is simulated numerically using the commercial CFD code FLUENT based on the VOF technique. Three high Reynolds number turbulence models have been considered: the standard k-ε model, realizable k-ε model, and Reynolds Stress model.

The results can be summarized as follows.

According to the experimental results of the flow patterns observed by Shakouchi *et al*. [4] and Iguchi *et al*. [9], the kinetic energy contours for these two configurations (h = 1 cm, and h = = 0.2 cm with Q_w = 50 cm^3/s) are as expected.

The realizable k-ε model is found to be more accurate than the standard k-ε and Reynolds Stress model in predicting the center line velocity profile. The discrepancies observed for h = 1 cm at z > 15 cm are due to the buoyancy effect which is not well captured in this simulation. So as to avoid this problem, the other two phase models can be proposed in further work.

The center line kinetic energy profile is over predicted by the Reynolds stress model and slightly under predicted by both standard and realizable k-ε models. Calculated flow patterns of the realizable k-ε model match well with experimental measurements of Iguchi *et al.* [9]. The inadequacy of the Reynold stress model to describe the velocity and turbulent kinetic energy could be due to the assumptions of the homogeneous two phase model. Nevertheless, further investigations using more elaborate and sophisticated models are needed.

NOMENCLATURE

D – vessel diameter, [m]
d – jet diameter, [m]
L – duct jet length, [m]
g – acceleration due to gravity, [ms^{-2}]
h – distance from the jet exit to the bath free surface, [m]
u – axial mean velocity, [ms^{-1}]
l – turbulent length scale, [m]
p – fluid pressure, [kgm^{-1}s^{-1}]
ε – energy dissipation rate, [m^{2}s^{-3}]
k – turbulent kinetic energy, [m^{2}s^{-2}]
z – vessel depth coordinate, [m]

Greek letters

μ – viscosity, [kgm^{-1}s^{-1}]
ρ – density, [kgm^{-3}]
σ – interfacial tension, [kgm^{2}s^{-2}]
Φ – scalar variable, [–]
φ – liquid primary-phase volume fraction, [–]

Subscripts

inlet – at the inlet of the jet
outlet – at the outlet flow
g – relative to the gas (air)
l – relative to the liquid (water)

REFERENCES

[1] Bin, A. K., Gas Entrainment by Lunging Liquid Jets, *Chemical. Engineering. Science., 48* (1993), 21, pp. 3585-3630
[2] Chanson, H., Cumming, P. D., Modeling Air Bubble Entrainment by Plunging Breakers, *Proceeding*, (Eds. M. Isaacson, M. Quick), International Symposium: Waves – Physical and Numerical Modeling, IAHR, Vancouver, Canada, Vol. 2, pp. 783-792, 1994 (ISBN 0-88865-364-6)
[3] Chanson, H., Air Bubble Entrainment in Free-Surface Turbulent Shear Flows, Academic Press, London, UK, 1997
[4] McKeogh, E. J., Ervine, D. A., Air Entrainment Rate and Diffusion Pattern of Plunging Liquid Jets, *Chemical Engineering Science, 36* (1981), 21, pp. 1161–1172
[5] Van de Donk, J., Water Aeration with Plunging Jets, Ph. D. thesis, TH Delft, The Netherlands, 1981
[6] Bonetto, F., Lahey, R.T. Jr, An Experimental Study on Air Carryunder due to a Plunging Liquid Jet, *Intl J. of Multiphase Flow, 19* (1993), 2, pp. 281-294
[7] Wood, I. R., Air Entrainment in Free-Surface Flows, IAHR Hydraulic Structures Design Manual No. 4, Hydraulic Design Considerations, Balkema, Rotterdam, The Netherlands, 1991
[8] Shakouchi, T., Akita, T., Ota, H. Sato, S., The Flow Characteristics of Round Water Jet (in Japanese), 15th Multiphase Flow Symposium 1996, Fukui, Japan, pp. 101-104
[9] Iguchi, M., Okita, K., Mean Velocity and Turbulence Characteristics of Water Flow in the Bubble Dispersion Region Induced by Plunging Water Jet, *Int. J. Multiphase Flow, 24* (1998), 4, pp. 523-537
[10] Scheuerer, M., Selection of PTS-Relevant Test Cases, 5th Euratom Frame Work Programme 1998-2002 – Key action: Nuclear Fission
[11] Hirt, C. W., Nichols, S. D., Volume of Fluid (VOF) Method for Dynamics of Free Boundaries, *J. Computational Physics., 39* (1981), 1, pp. 201-225
[12] Launder, B. E., Spalding, D. B., The Numerical Computation of Turbulent Flows, *Computer Methods in Applied Mechanics and Engineering, 3* (1974), pp. 269-287
[13] Bousbia Salah, A., Moretti, F., D'Auria, F., State of the Art and Needs for Jet Instabilities and Direct Contact Condensation Model Improvements, *Nuclear Technology and Radiation Protection, 22* (2007), 1, pp. 58-66

Received on April 2, 2009
Accepted on March 22, 2010

Фаиза ЗИДУНИ КЕНДИЛ, Анис БУСБИЈА САЛАХ, Амина МАТАУИ

ПРОЦЕНА УЧИНАКА ТРИ МОДЕЛА ТУРБУЛЕНЦИЈЕ ЗА ПРЕДВИЂАЊЕ ТОКА ВОДЕНОГ МЛАЗА КОЈИ УРАЊА У БАЗЕН СА ТЕЧНОШЋУ

Основна намера овог проучавања је да рачунарским моделовањем динамике флуида нумерички испита водени млаз убризган кроз праву цев вертикално наниже у базен са водом. Циљ је такође, боље разумевање понашања млаза, уношења ваздуха и дисперзије мехурања у области тока који се развија. У ову сврху, техником запремине флуида, тродимензионално су моделовани ваздушни и водени токови. Потребне једначине формулисане су коришћењем густине и вискозности "гасно-течне мешавине", описане појмовима фазно запреминске фракције.

За дати ток разматрана су три модела турбуленције са великим Рејнолдсовим бројем: стандардни *k-ε* модел, оствариви *k-ε* модел и Рејнолдсов стрес модел. Предвиђени обрасци тока по остваривом *k-ε* моделу добро се слажу са експерименталним мерењима наведеним у литератури. Ипак, нека неслагања која се тичу слабљења брзине и расподеле момента турбуленције у базену морају бити споменута, и за стандардни *k-ε* и за Рејнолдсов стрес модел.

Кључне речи: водени млаз, урањање, моделовање турбуленције, модел запремине флуида, остваривi k-ε модел, Рејнолдсов стрес модел, стандардни k-ε модел